FPGA-Based High-Speed Optical Fiber Sensor Based on Multitone-Mixing Interferometry

Javier Elaskar, Marcelo A. Luda, Lorenzo Tozzetti, Jorge Codnia, and Claudio J. Oton

***Abstract*— We report a real-time high-speed fiber Bragg grating (FBG) interrogator based on a fiber-optic interferometer. The signal processing is performed by using a low-cost field-programmable gate array (FPGA) system, which is programed to implement a phase-generated carrier (PGC) demodulation algorithm with multitone mixing (MTM) to provide distortion-free signals with high tolerance to modulation depth variations and light intensity fluctuations. The system can stream data at rates up to 1 MS/s and allows multiplexed processing up to two channels. Experimental results show simultaneous measurements of two FBGs, one of which was actuated at frequencies up to 100 kHz. The system features a 3-dB bandwidth of 280 kHz, and a dynamic wavelength resolution of 4.7 fm/Hz$^{1/2}$. We also demonstrate a strong reduction of distortion using the MTM approach with respect to the standard technique. Finally, we study the origin of the noise, demonstrating a reduction in common noise sources by using one of the FBGs as a reference. The system can measure FBGs centered at any position within the spectral band of the source, is polarization-independent, and is easily scalable to more than two measurement channels from the same interferometer.**

***Index Terms*— Fiber Bragg gratings (FBGs), interferometers, optical fiber sensors, phase demodulation, phase-generated carrier (PGC), strain sensors, vibration sensors.**

I. Introduction

OPTICAL fiber sensors are devices in which the transducer of the physical magnitude to measure is the optical fiber itself [1]. This technology has many advantages with respect to purely electronic transducers, such as immunity to electromagnetic interference, small size, tolerance to harsh environments, and the possibility of using the same optical fiber to transmit the optical information to an interrogator which can be situated in a remote place; but probably the most important advantage is the possibility to multiplex many sensing points along one single fiber cable, enabling distributed or quasi-distributed measuring schemes [2].

Manuscript received October 18, 2021; revised February 10, 2022; accepted March 25, 2022. Date of publication April 7, 2022; date of current version April 20, 2022. This work was supported by the Italian Space Agency [Agenzia Spaziale Italiana (ASI)] through the Project Photonic Real-Time Analyzer for Distributed Monitoring in Aerospace (ARTEMIDE), within the initiative "Nuove idee per la Componentistica Spaziale del Futuro TRL." The Associate Editor coordinating the review process was Dr. Kok-Sing Lim. *(Corresponding author: Javier Elaskar.)*

Javier Elaskar, Lorenzo Tozzetti, and Claudio J. Oton are with the Department of Excellence for Robotics and Artificial Intelligence, Institute of Mechanical Intelligence, Scuola Superiore Sant'Anna, 56124 Pisa, Italy (e-mail: javierdario.elaskarplazas@santannapisa.it).

Marcelo A. Luda and Jorge Codnia are with CEILAP, CITEDEF, Buenos Aires 1603, Argentina.

Digital Object Identifier 10.1109/TIM.2022.3165291

One very popular type of optical fiber sensor is the fiber Bragg grating (FBG), which is a periodic modulation of the refractive index in a certain position, which generates a narrow optical reflection peak. The precise wavelength of the peak can depend on physical parameters, such as temperature and strain, and depending on how the fiber is implemented, it can also respond to pressure, force, etc. To read the peak positions in real time coming from the fiber, a so-called FBG interrogator is needed. Interrogators are commercially available from many different providers, and they are typically based on swept lasers or spectrometers with a white light source. However, these schemes for reading the wavelength require a certain time to perform each measurement, which is limited by the laser scanning time or the readout time of the spectrometer. Typical FBG interrogators read at rates of few kHz, with the fastest ones reaching few tens of kHz. However, some applications require much faster sampling rates, for example, when monitoring vibrations of fast-rotating machines, like gas turbines, explosion-based machines, such as combustion engines, or in ultrasound applications. These devices may require hundreds of kHz of bandwidth, which is very challenging using these techniques.

One way to monitor FBGs at high speed is to convert wavelength to intensity using a linearly shaped filter [3]. However, this technique is sensitive to intensity noise, has a very limited range, and can only measure FBGs that are spectrally aligned to the specific filter. To solve these issues, unbalanced interferometers can be used, as they can convert a wavelength shift to a phase shift. However, to get a good responsivity, they must be kept in quadrature, which can be challenging if many peaks must be read simultaneously from the same interferometer. To tackle this problem, the interferometer can be dithered continuously with a sinusoidal wave at a certain frequency f and the phase can be measured by extracting the components in f and $2f$, using the well-known phase-generated carrier (PGC) technique [4], [5]. To reach modulation frequencies in the MHz range, in [6], a lithium-niobate modulator within a Sagnac interferometer was used to demonstrate FBG interrogation at a bandwidth of 100 kHz.

On the other hand, the standard PGC technique can generate distortions when the modulation depth deviates from its nominal value. To solve that issue, many methods have been proposed in the past [7]–[11], but these methods have some disadvantages such as increasing noise around certain phase regions, requiring signal variations to work, or requiring complex ellipse-fitting algorithms. In [12], a method called

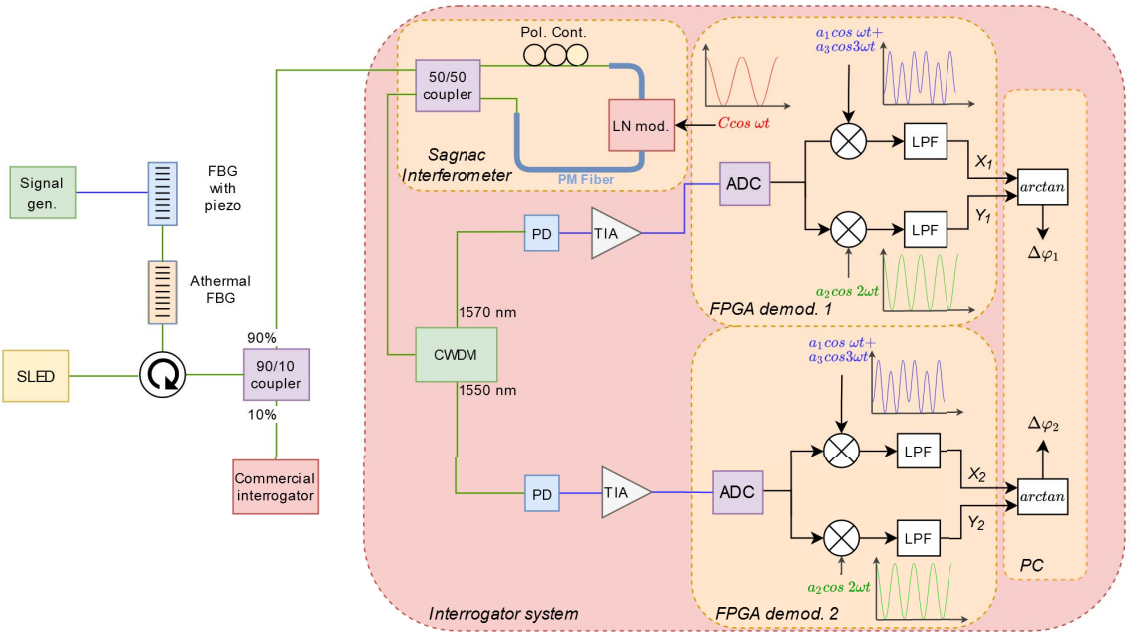

Fig. 1. Schematic of the optical system. LN: Lithium Niobate, PD: Photodetector, TIA: Transimpedance amplifier, LPF: Low-pass filter, SLED: Superluminescent light-emitting diode, PM: Polarization-maintaining, ADC: Analog-to-digital converter, CWDM: Coarse wavelength division multiplexer.

multitone mixing (MTM) was proposed which consists of the substitution of the sinusoidal functions for the mixing with synthetic functions that include up to the third or fourth harmonic, in such a way that the first- and second-order dependencies on the modulation depth are suppressed. That method, which is very easy to implement in a digital signal processing system, demonstrated to correct distortions in real time with no noise penalties. However, in that article, the technique was not demonstrated in real time, but only after post-processing.

In this article, we show the implementation of the MTM scheme on a low-cost field-programmable gate array (FPGA) and we demonstrate real-time FBG interrogation on an active Sagnac fiber interferometer at sample rates up to 1 MS/s and a bandwidth of 280 kHz. In addition, we demonstrate multiplexed reading from the same interferometer, which can also compensate the thermal fluctuations of the Sagnac by using one signal as a reference channel.

This article is divided as follows: in Section II, we first describe the optical setup, followed by a brief explanation of the MTM technique with its advantages, and finally an explanation of how the generation of the modulating signal and the demodulation system was implemented in the FPGA. In Section III, we discuss and analyze the obtained results; first, we compare our interrogator against other commercially available interrogators, then we show the advantages of using a second FBG as a reference, followed by a demonstration of the robustness of the MTM technique against the standard PGC, and finally, we show how it is possible to easily adjust the free spectral range (FSR) of the interferometer to be tailored according to the intended application. Finally, in Section IV, we draw a conclusion.

II. System Details

A. Optical Setup

Fig. 1 shows the optical system. The optical source is a fiber-coupled superluminescent light-emitting diode (model Denselight DL-BZ1-CS5169A), with an output power of 12 dBm, centered at 1550 nm, and with a 3-dB bandwidth of 80 nm. The broadband signal is sent to the FBGs. FGB#1, is an athermally packaged FBG, centered at 1571 nm, with FWHM 0.28 nm. FBG#2 centered at 1548.7, with FWHM 0.14 nm, was attached to a piezoelectric actuator providing a tuning range of 1.4 nm. The reflected peaks were split with a 90/10 ratio, where 10% was sent to the reference interrogator (Ibsen Photonics I-MON-512-USB). The reason why only 10% was sent to the reference interrogator was to avoid saturation. Another reference interferometer used was a Micrometer Optics Hyperion model Si155, although this one had its own source, it could not measure simultaneously with our system. For this reason, measurements acquired with this interrogator were taken before or after an interval of few minutes, while measurements acquired with the Ibsen interrogator are simultaneous with the traces acquired with the interferometric interrogator.

The 90% remaining signal was sent to the interferometer, which is a fiber-optic active Sagnac interferometer as described in [6]. The interferometer features a birefringent section to generate a polarization retardation that constitutes the optical path difference of the interferometer. In our case, the birefringent section consists of a lithium niobate modulator (model Ixblue MPX-LN-0.1), and polarization-maintaining fibers (PMFs) that come out of the modulator. The Sagnac loop also has a single-mode fiber (SMF) section with a polarization

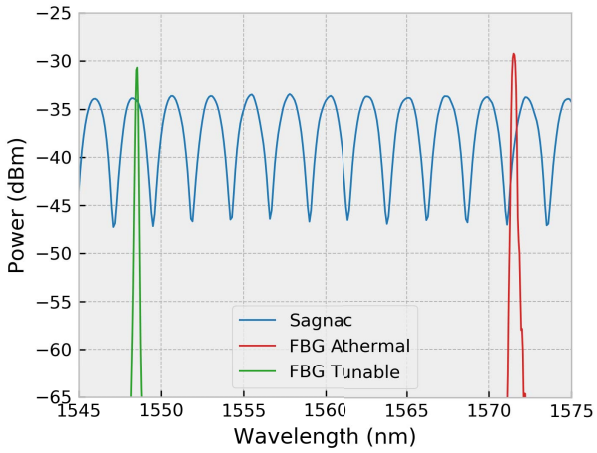

Fig. 2. Spectra of Sagnac interferometer for 7 m (2 + 5 m extension) of PMF, generating a fringe pattern with an FSR of 2.37 nm (blue) and reflection spectra of FBGs (red and green). OSA resolution: 0.1 nm.

controller, which is used to align the polarizations at 90° between the coupler ports to maximize the fringe contrast. Once the polarization controller is adjusted, the interferometer is polarization-independent, as neither the fringe positions nor their contrast depend on the input polarization.

The system generates a fringe pattern whose FSR is determined by the total retardation, as shown below [6]:

$$\Delta\nu_{\mathrm{FSR}} = \frac{c}{\Delta n_{\mathrm{LN}} L_{\mathrm{LN}} - \Delta n_{\mathrm{PMF}} L_{\mathrm{PMF}}} \tag{1}$$

where $\Delta\nu_{\mathrm{FSR}}$ is the optical frequency FSR, Δn_{LN} is the optical birefringence of lithium niobate (equal to 0.0735 at 1550 nm [13]), L_{LN} is the length of the modulator, Δn_{PMF} is the birefringence of the PMF (equal to $\sim 4 \times 10^{-4}$ in our case, a typical panda fiber), and L_{PMF} is the total length of the PMF section in the system. The minus sign is due to the fact that the PMF is pigtailed to the LN modulator so that the slow axis is aligned to the electric field direction in the modulator, which is the typical case. This allows us to generate any FSR in our interferometer by varying the length of the PMF pigtail of the modulator. In our case, we generated an FSR of 0.94 nm by prolonging the 2-m pigtails by an extra meter, while prolonging with 5 m generated an FSR of 2.37 nm. The advantage of this interferometer is that the position of the fringes can be electro-optically tuned at the bandwidth of the LN modulator, which can reach the GHz range. In our setup, the modulation signal of the interferometer was a sinusoidal wave at 2.6 MHz. The spectra of the interferometer with 7 m of PMF and the FBGs are shown in Fig. 2. Each spectrum was measured separately, without applying any modulation signal. The measured insertion losses of the Sagnac interferometer were 6 dB.

Finally, the output of the Sagnac interferometer was demultiplexed with a four-channel coarse wavelength division (de)multiplexer (CWDM), model WDM Cubo, Part C40-A-A-S-S-11. With that device, we separated the signals coming from FBG#1 and FBG#2 using the channels centered at 1571 and 1551 nm. The signals were sent to two InGaAs photodiodes (model PD-LD PDINP0751FAA-0-0-01) and converted to voltage with two transimpedance amplifiers model Femto DHPCA-100, set to a gain of 10^5 with ac coupling, with a bandwidth of 14 MHz. These signals were then sent to the FPGA to be processed.

The optical system can be easily extended to N FBGs without the need of much extra complexity, since it would only require a WDM with one channel per FBG and one photodetector per channel, without any modification to the Sagnac interferometer. It could also be used for spatial multiplexing, with M channels, each with N FBGs, only by setting the Sagnac interferometer immediately after the light source and then splitting the interferometric pattern to the M channels with a splitter. This setup was not used in our system since we needed the FBGs immediately after the light source so that we could compare the results with a commercial interrogator.

B. MTM Technique

In order to determine the wavelength shift from the interferometer output, one has to measure the phase shift of the interferometer, divide it by 2π, and multiply it by the FSR in wavelength as follows:

$$\Delta\lambda = \frac{\Delta\varphi}{2\pi}\Delta\lambda_{\mathrm{FSR}}. \tag{2}$$

To extract the phase of the interferometer with no responsivity fading, one can dither the interferometer with an oscillating signal at a frequency ω. By doing this, the optical intensity output of the interferometer becomes

$$I(t) = A + B\cos[C\cos(\omega t) + \varphi(t)] \tag{3}$$

where $I(t)$ is the signal intensity, A and B are coefficients depending on the fringe contrast, C the modulation depth, and $\varphi(t)$ is the phase of the peak position within the fringe pattern defined in (2).

This output can be expanded using the Bessel functions [4]

$$I = A + B\left\{\left[J_0(C) + 2\sum_{k=1}^{\infty}(-1)^k J_{2k}(C)\cos 2k\omega t\right]\cos\Delta\varphi(t) - \left[2\sum_{k=0}^{\infty}(-1)^k J_{2k+1}(C)\cos(2k+1)\omega t\right]\sin\Delta\varphi(t)\right\} \tag{4}$$

where J_i represents the Bessel function of the first kind. This means that even harmonics of the signal contain the in-phase term of the phase [proportional to $\cos(\Delta\varphi)$], while the odd harmonics contain the quadrature component [proportional to $\sin(\Delta\varphi)$].

The standard PGC typically applies a modulation depth $C_{\mathrm{nom}} = 0.84\pi$, which makes the Bessel function $J_1(C) = J_2(C)$, so that the phase can be calculated from the first and second harmonics of the signal

$$\Delta\varphi_{\mathrm{PGC-std}}(t) = \arctan\left[\frac{I_\omega}{I_{2\omega}}\right] \tag{5}$$

where I_ω and $I_{2\omega}$ are the components of the signal in ω and 2ω, respectively. However, deviations of the modulation

depth C can occur due to different reasons, like thermal fluctuations that affect the digital-to-analog converter (DAC) of the signal generator or the responsivity or the modulator, a change in the modulation frequency setting, or simply that the fact that the responsivity of the electrooptic modulator also depends on wavelength, which would make it impossible to fix a modulation depth for all wavelengths simultaneously. When the modulation depth deviates from the nominal value, the phase extraction is subject to distortion, which generates a phase inaccuracy and undesired harmonics. To solve this problem, instead of mixing with pure sinusoidal waves at frequencies ω and 2ω, in [12] it was proposed to mix with synthetic signals F_1 and F_2 defined as follows:

$$F_1(t) = a_1 \cos \omega t + a_3 \cos 3\omega t \tag{6.a}$$

$$F_2(t) = a_2 \cos 2\omega t + a_4 \cos 4\omega t. \tag{6.b}$$

For a given nominal modulation depth, choosing the coefficients $a_{1,\ldots,4}$ to minimize the derivatives of the Bessel function combinations, using F_1 and F_2, the phase can be calculated as follows:

$$\begin{aligned}\Delta\varphi_{\mathrm{MTM}}(t) &= \arctan\left(\frac{I \otimes F_1}{I \otimes F_2}\right) \\ &= \arctan\left[\frac{[a_1 J_1(C) - a_3 J_3(C)]\sin\Delta\varphi}{[a_2 J_2(C) - a_4 J_4(C)]\cos\Delta\varphi}\right] \\ &= \arctan\left(\frac{Y}{X}\right)\end{aligned} \tag{7}$$

where $I \otimes F_1$ and $I \otimes F_2$ are results of the mixing and low-pass filtering the light intensity function $I(t)$ with functions F_1 and F_2, respectively. For the specific case which excludes 4ω (which is recommended when $C < \pi$, as it minimizes noise [12]) and for the nominal modulation depth of $C_{\mathrm{nom}} = 0.84\pi$, the coefficients that minimize distortion are $a_1 = 1$, $a_2 = 2.5806$, $a_3 = -3.03391$, and $a_4 = 0$. This is because by using the appropriate coefficients, the functions in the numerator and denominator in (7) can be tailored in such a way that the distortion is minimized when $C \neq 0.84\pi$ [12].

The advantage of the MTM scheme, with respect to other techniques proposed in the past to reduce distortion, is the fact that its implementation requires a minimal modification of the system, as it only requires the modification of the pure tone waves with synthetic signals for the mixing.

C. FPGA Design

The MTM phase measurement algorithm was implemented in a real-time processing scheme that involves an FPGA design for the acquisition and in-phase and quadrature demodulation, in a first stage, and then computer software for the trigonometric calculus and data storage.

The hardware design was built in a Red Pitaya STEMlab 125-14 device, based on a Xilinx Zynq 7010 integrated circuit, that includes FPGA and a dual core ARM Cortex-A9 processor, and comes with an Ethernet port for network connection. The device runs a Linux operating system (OS) that works as an interface between a remote control computer and the programmable hardware layer.

The main advantage of this board choice is that it incorporates two analog-to-digital converters (ADCs), whose input buses are labeled as **in1** and **in2** in the present work, and two DACs, identified as **out1** and **out2**. All of them have a 14-b resolution for $\pm$1-V range and are operated at 125-MS/s rate, much higher than the sample rate of analog signals achievable by other embedded devices options, like Arduino or Raspberry Pi. The input–output operations are synchronized with the main internal clock of the FPGA layer, **clk**, which also works at a frequency $f_0 = 125$ MHz.

The Red Pitaya project provides some useful tools that ease the building of a user operation interface for the designed circuit, delivered as open-source code. For example, it includes an AXI interface implemented to map chosen FPGA registers to the RAM of the OS, so they can be read and written using the standard memory operation form software. The values of these registers are used to control the behavior of the implemented logic or to read out the result of the MTM data processing. The board includes an environment with a web server that lets the user change the register values from a remote device using POST and GET queries. The open-source code includes HTML interfaces that make these operations and organize the data for visualization. These tools were successfully used in previous work for the implementation of a lock-in amplifier in the same device [14]. Some parts of the present work design are based on the code of the aforementioned one.

The FPGA layer was designed in Verilog language and synthesized using Xilinx Vivado 2015.2 software. The design of the MTM demodulation module is shown in Fig. 3. The thick lines are data buses and the thin ones are clock lines. The gray blocks are 14-b read-only memory arrays that store values of the harmonic functions used for modulation and demodulation. The read address of each one is fed by cyclic counters whose step time is controlled through a frequency divider **div** applied to **clk** signal. It is implemented as a module that outputs a tick bit after counting **step** cycles of **clk** (see Fig. 4). This signal feeds the input of the master counter, **cnt**, which is used to establish the base time for the 14-b **cos_ref** reference signal, defined with 48 values. In this way, the **cos_ref** memory has a reading sample rate of f_0/**step** and the harmonic signal has a maximum frequency of $f_0/48 =$ 2.6 MHz (for **step** $= 1$). The signal can be assigned to **out1** and its output amplitude can be regulated by multiplication with **mod** register.

The internal demodulation signals **cos_[n]f** are produced in a similar way. Each one is stored in a memory array whose read address is controlled by the corresponding **cnt[n]** counter. To provide phase control with respect to **cos_ref**, we use the registers **phase** and **phase_f**. A comparator module **cmp** sets each counter to zero by sending a reset tick delayed respect to the event **cnt** $= 0$ (the **cos_ref** start). This delay is produced by waiting a **phase** number of **div** ticks and **phase_f** ticks of **clk** (see Fig. 4). In this way, we have a coarse control of the demodulation phase offset, with $2\pi/48$ steps, and a fine control of 2π **phase_f**/(48*__step__). Moreover, the input of each counter is produced by the **delay** module that copies the **div** signal to the output after **phase_f** ticks of **clk**. The **cos_[n]f** signals are

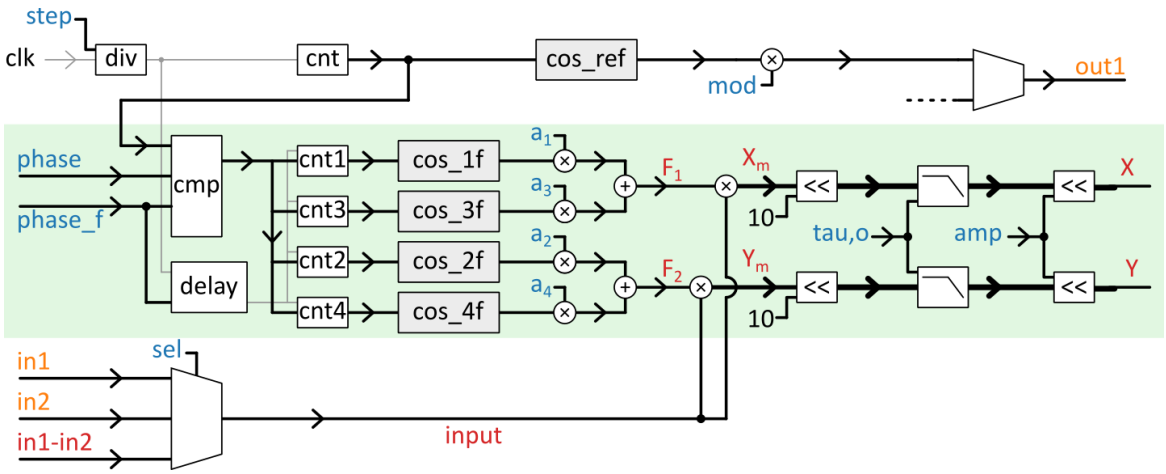

Fig. 3. Simplified scheme of the FPGA design for MTM demodulation. Thin lines are clock lines and the thick ones are data buses of 14-, 28-, and 38-b length on width order. Blue labels are user real-time configurable registers. Red labels are the names of internal signals that can be visualized by an oscilloscopic interface. Gray blocks are memory arrays whose read address input is fed by synchronized counters that can be de-phased through phase registers. The "≪" blocks are configurable shift registers that expand the data bus on the least significant side. When the output of a product has the same bus width than the input, a shift register division should be assumed to keep the bus width.

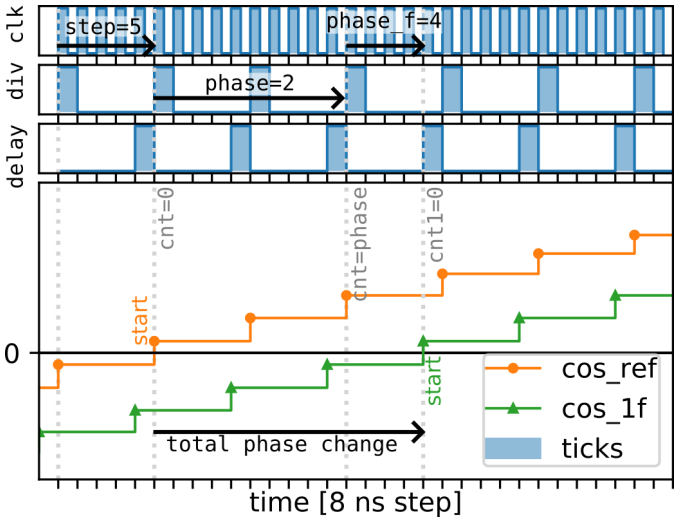

Fig. 4. Phase relationship between cos_ref and cos_1f signals. The first row represents the main clock signal, clk. The second one represents the output of the frequency divider, div, that outputs a tick after step cycles of clk. The output of delay module is a copy of div output delayed by phase_f steps of clk. In the last row, the outputs of the memory modules are depicted. The event cnt = 0 marks the start of the cos_ref signal. The cmp module sets cnt1 = 0 after the configured delay time, producing the (re)start of the cos_1f signal.

multiplied by $\mathbf{a_n}$ register values and summed, following the combination from (6) to build the $\mathbf{F_1}$ and $\mathbf{F_2}$ internal signals. These are multiplied by the input signal, that can be selected through a multiplexer, and build up $\mathbf{X_m}$ and $\mathbf{Y_m}$ products.

To complete the demodulation scheme the product signals are processed by two low pass filter (LPF) modules. Each one is composed by four blocks of first-order filters concatenated, achieving the net effect of a single filter of up to fourth order. The **o** register (see Fig. 3) lets the user choose to bypass or not each of them and control in this way the final order of LPF module. Each block contains an infinite impulse response (IIR) filter of first order based on (8a). There, **y[i]** is the output, **in[i]** is the input, and $\alpha = dt/(\tau + dt)$, where dt is the **clk** step time (8 ns) and τ is the characteristic time of the LPF

$$y[i] = y[i-1] + \alpha(\text{in}[i] - y[i-1]) \tag{8a}$$

$$Y[i] = Y[i-1] + \text{in}[i] - Y[i-1]/\beta. \tag{8b}$$

The FPGA layer was designed to use integer values in the data buses and its operations. α is a rational number, so instead of (8a), the implementation was made using (8b), where $\mathbf{Y} = \beta\mathbf{y}$, $\beta = 1/\alpha = 2^{\mathbf{tau}}$, and **tau** is a register for user configuration. The products and divisions by powers of two are implemented using the shift register operation, where the shift number is defined by **tau**. In this way, by setting the **tau** register, the user can change the characteristic time of the LPF: $\tau = (2^{\mathbf{tau}} - 1) \cdot 8$ ns. As a result, the complete module has a configurable frequency cut-off $f_c = 1/(2\pi\tau)$ between 2.8 MHz and 75 Hz (for τ = 3–18).

Before the LPF modules, we make a $\times 1024$ amplification through a shift register operation ($\ll 10$) to enhance the resolution of the demodulation by averaging effect. This adds 10 b on the least significant side of the data bus that is populated by the LPF module, enabling the possibility to demodulate signals with amplitudes much lower than the ADC minimal measurable voltage. Then, we apply a configurable $\times 2^{\mathbf{amp}}$ amplification. Finally, a 14-b trimming of the most significant bits produces the quadrature signals **X** and **Y**, suitable for trigonometric processing. With this scheme, we achieved a final net amplification up to $\times 2^{19}$.

The green box shown in Fig. 3 was instantiated twice, so the implementation has two demodulation lines. The orange labels shown in Fig. 3 are connections to input and output peripherals. The blue ones are configurable registers that let the user control the behavior of the demodulation circuit in real time. The red label signals are wired to an oscilloscope module for acquisition and visualization. The designs of the demodulation procedure, the LPF modules, and the oscilloscope module are similar to that used in [14], whose code was already published.

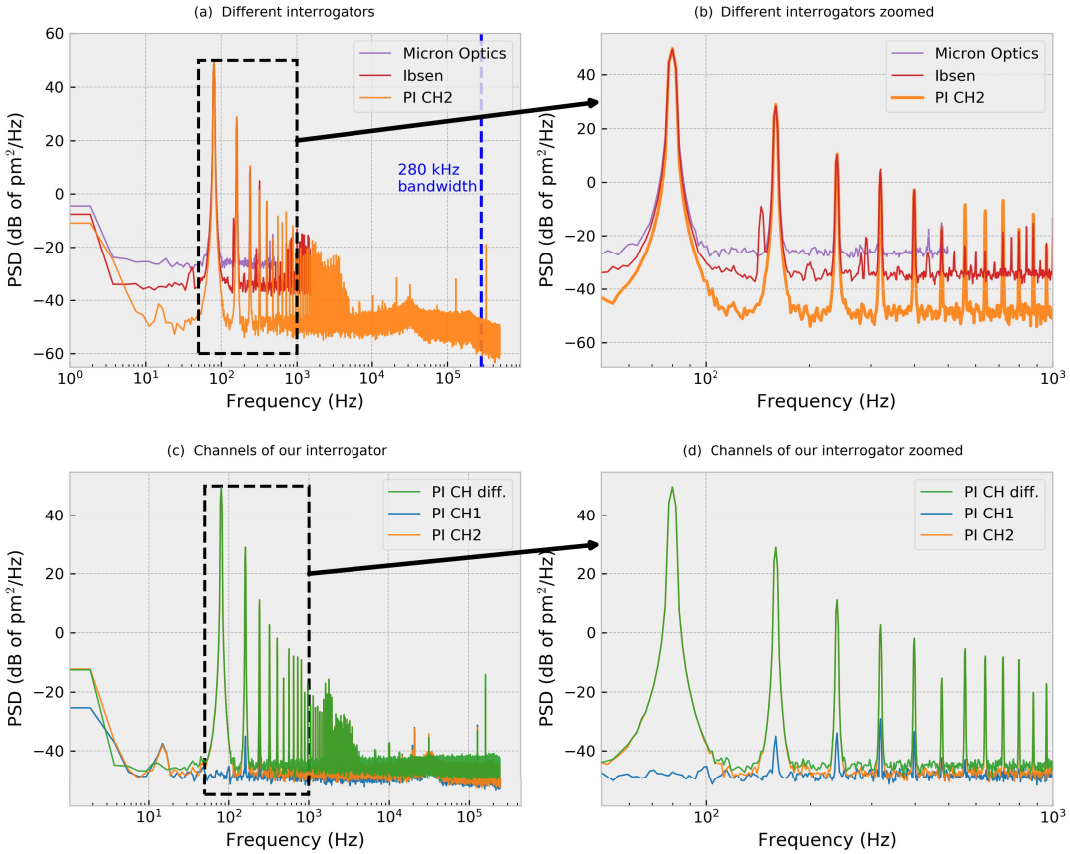

Fig. 5. PSD of a wavelength shift applying a sine signal at 80 Hz for different configurations with 5 s of acquisition time. PI: Proposed interrogator. CH: channel. In (a) and (b), we compare our proposed interrogator (at 0.98 MS/s acquisition rate) with two commercial instruments. In (c) and (d), we show channels one and two of our interrogator and their difference (at 0.49 MS/s acquisition rate per channel). (a) Different interrogators. (b) Different interrogators zoomed. (c) Channels of our interrogator. (d) Channels of our interrogator zoomed.

The oscilloscope module consists of two memory arrays with 16 384 elements of 14-b integer data that are written in order of arrival from two selectable input buses. A **dec** register lets the user configure the decimation of the acquired signal using a frequency divider f_0/**dec** to command the writing operations. In addition, at the input of the module, there is an averaging filter (that can be switched ON/OFF) to avoid aliasing effects. The **dec** values are powers of two, so that the averaging can be implemented with an accumulator and a shift register operation for the division. The final acquisition sample rate that the user can achieve for the demodulation signals would then be $125/2^n$ MS/s, with integer n.

We made two interfaces for remote control of the designed circuit and for data acquisition. The first one is an interactive web page that can be loaded from the server of Red Pitaya device and communicate with it through standard HTTP queries. It is based on the examples published as open-source by the Red Pitaya project [15] and is similar to the one developed in [14]. The second one is an HTTP API that lets the user read and write the registers of the circuit using GET queries to the web server. This enables the operation of the device using any general-purpose programming language from a remote computer.

One of the desired characteristics of the system is the possibility to make long continuous acquisitions of the demodulated signals. For this purpose, we made a computer program in *C* that runs in the native Red Pitaya Linux OS. It continuously reads the oscilloscope memory buffer and streams it to the remote user computer. This implementation has a bottleneck in the computer's local process reading speed, limited by the kernel scheduler and the hardware interruptions. After some tests, we found that continuous data stream of the two oscilloscope channels could be made without data loss using **dec** $= 128$. With this parameter, the system can send up to f_0/**dec** $= 0.98$ MS/s, where each sample is composed by the two 14-b values of each oscilloscope channel.

To send one demodulation line, the oscilloscope inputs are configured to acquire the X output of the line in one channel and the Y output on the other one. Time multiplexing was used to send both demodulation lines at the same time, so the sample rate is half the maximum in that case. The streaming program can be launched and configured through the web application or the HTTP API. The streamed data is acquired, plotted, and stored in the user computer by a server software. We made two server software versions: one in *C* for simple file storage and one in LabView, with real-time visualization.

The whole implementation of the system, with the oscilloscope module, the two demodulation lines, and the AXI interface, use 9289 slice LUTs of the 17 600 available in the FPGA Zynq 7010 integrated circuit. The two demodulation

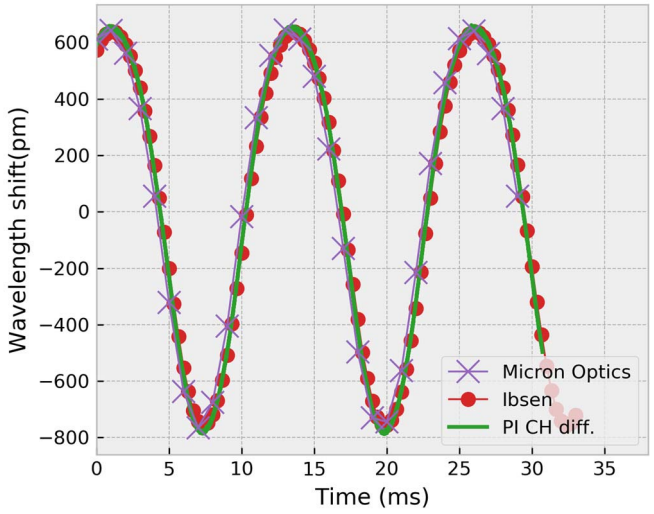

Fig. 6. Wavelength shift retrieved from different interrogators for a sine signal at 80 Hz. These time signals correspond to the spectra shown in Fig. 5(a) and (b).

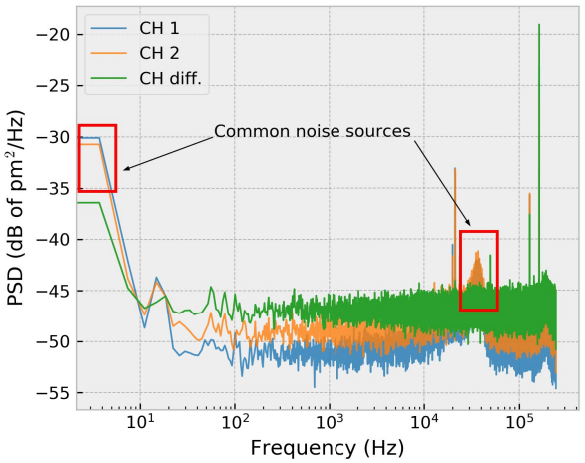

Fig. 7. Noise PSD of different channels of our interrogator. CH: channel. The calculated channel difference reduces the common noise sources at the expense of slightly increasing the noise floor.

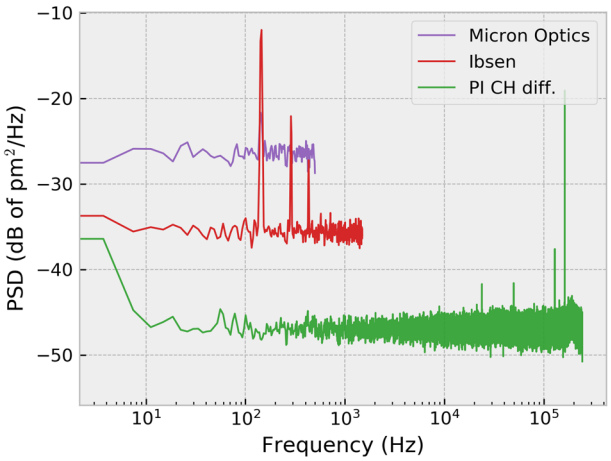

Fig. 8. Noise PSD for different interrogators. PI CH diff: Proposed interrogator subtracting channels 1 and 2.

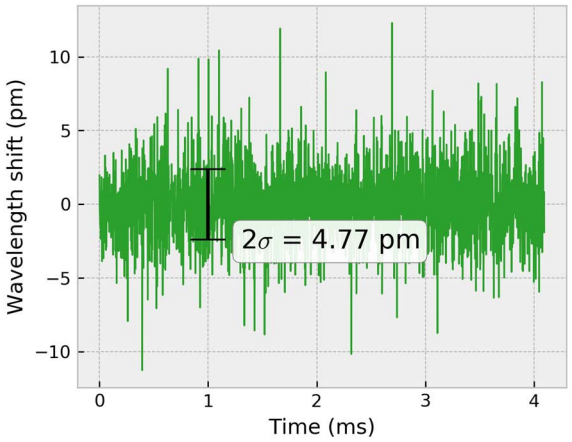

Fig. 9. Noise in the time domain of the channel difference of our proposed interrogator in absence of input actuating signal.

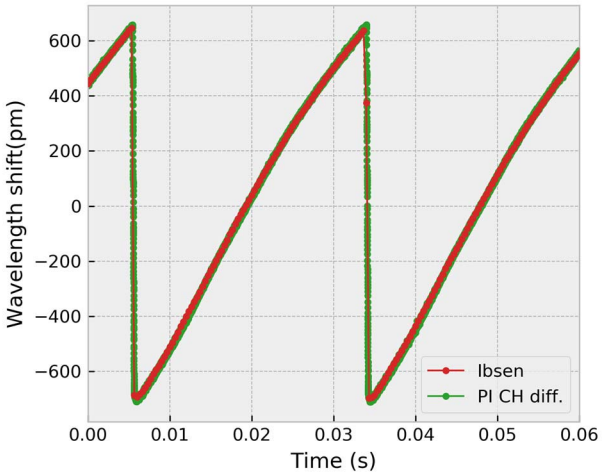

Fig. 10. Retrieved 35-Hz sawtooth signal from different interrogators. PI CH diff: Proposed interrogator channel difference.

lines consume 5732 slice LUTs, so theoretically, there are still resources to implement more lines if we add another ADC. Two more lines can be added using a second STEMlab 125-14 device with shared main clock signal.

To scale the system to N FBGs, it would require $N/2$ synchronized STEMlab 125-14, each with two demodulation lines. Otherwise, more complex hardware could be used as long as it has enough resources to demodulate N channels with N ADCs.

III. Experimental Results

A. Single Channel Acquisition

Fig. 5(a) and (b) shows a power spectral density (PSD) comparison among different interrogators when the FBG#2 is excited with a sine signal of 80 Hz. Our interrogator was first set to demodulate only channel 2, which allowed us to set the sampling rate at 0.98 MS/s. All the interrogators detect the same frequency at 80 Hz and its harmonics and are dominated by the nonlinearity of the piezoelectric actuator, which is

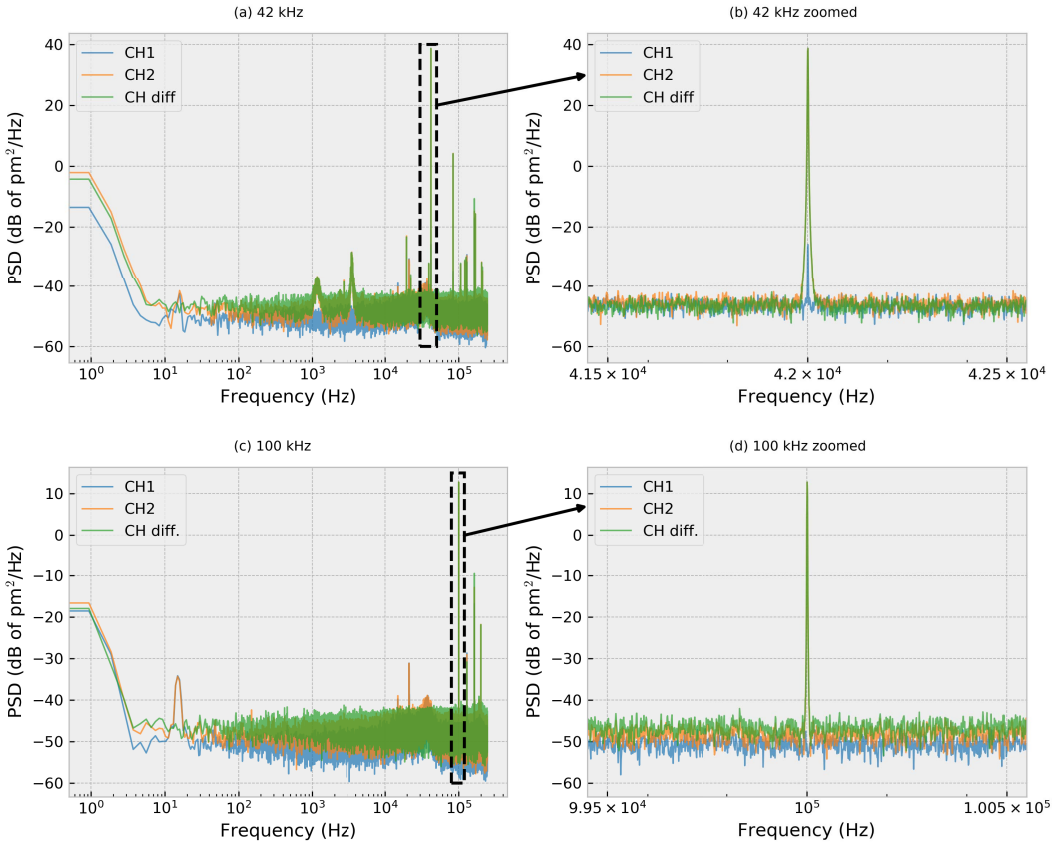

Fig. 11. PSD of sine signals at different frequencies retrieved from our interrogator. (a) 42 kHz. (b) 42 kHz zoomed. (c) 100 kHz. (d) 100 kHz zoomed.

why they appear in all three interrogators. Our proposed interrogator has a better SNR because of the lower noise floor and features a much wider bandwidth (up to 280 kHz) that allowed us to observe higher-order harmonics that the other interrogators are unable to detect.

B. Dual Channel Acquisition

Fig. 5(c) and (d) shows the PSD of the same 80-Hz signal, but only for our proposed interrogator, enabling both channels. In this case (and for all the following results), the sampling rate of the interrogator was reduced to 0.49-MS/s per channel to keep the same total transmission rate. One of the advantages of using a second FBG is that it can be used as a reference, as we did in this case, to eliminate any noise that is common to both received signals by means of subtracting the two signals in the time domain. Since FBG#1 was athermal and was not subject to actuation, when computing the difference between the FBGs, all the thermal noise generated in the interferometer was eliminated in this configuration, along with other common noise sources. Fig. 6 shows the retrieved signal from different interferometers when applying an 80-Hz sine signal to the FBG#2. There is a good agreement between the different traces, and there is a small phase delay between them since the traces were taken at different times, and then adjusted to match in time by introducing phase delays in post-processing.

Fig. 7 compares the noise for the different channels of our interrogator. Channel 1 had a slightly lower noise than channel 2, probably since FBG#1 FWHM is wider, therefore providing a higher optical signal intensity than FBG#2. When channels 1 and 2 are subtracted, many common noise sources (at frequencies below 10 Hz, and for some frequencies between 30 and 40 kHz) are reduced. However, the noise floor is slightly higher because the noise floors of each channel are uncorrelated.

Fig. 8 compares the noise levels of the computed channel difference from our interrogator with other interrogators. The noise floor of our interrogator is lower than the others (about 10 dB lower than the one with the lower noise floor). It is worth mentioning that the strongest noise peak, observed at a frequency of 162 kHz, is an aliased peak caused by the modulation frequency $f_{\text{mod}} = 2.6$ MHz and a sampling rate $f_{\text{s}} = 0.49$ MS/s, as $f_{\text{mod}} - 2f_{\text{s}}$ precisely equals 162 kHz.

Table I shows the noise levels and dynamic resolutions of the three interrogators, which show that our system has a dynamic wavelength resolution of 4.7 fm/Hz$^{1/2}$, which is a factor of ∼10 and ∼4 lower than the Micrometer Optics and the Ibsen, respectively. Fig. 9 shows the temporal trace of the noise, with the calculation of the standard deviation $\sigma = 2.39$ pm at full bandwidth (280 kHz). This value is actually higher than σ measured with the commercial interrogators, but that is because the bandwidths are very different. Low-pass filtering the trace to achieve equal bandwidth would reduce the noise proportionally to the square root of the bandwidth.

Fig. 10 shows a sawtooth signal at 35 Hz retrieved from our interrogator and a commercial one. For comparison, the

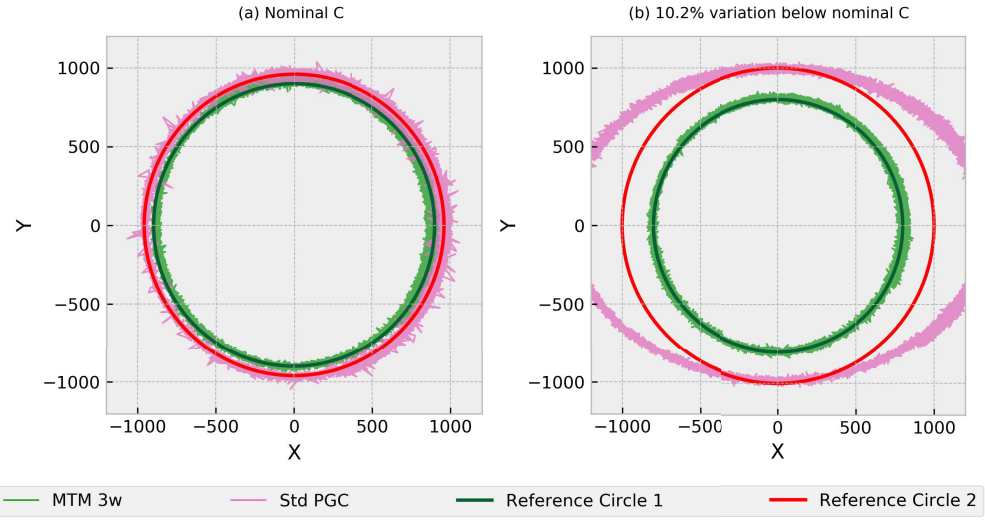

Fig. 12. Plot of Y versus X components for the MTM and standard PGC techniques, for different modulation depths (C). MTM $3w$: MTM up to $3w$. Std PGC: Standard PGC. X and Y do not have units as they are retrieved from digital values, and it is only of interest for comparison between them. As C drifts from its nominal value, the circle shape from Std PGC starts to transform into an ellipse, which means that distortion is introduced in the retrieved signal. However, for the MTM technique, the circle keeps its original shape, therefore it is almost unaffected by changes in C for small variations. (a) Nominal C. (b) 10.2% variation below nominal C.

TABLE I
COMPARISON AMONG DIFFERENT INTERROGATORS

Model	Bandwidth (kHz)	Noise floor (dB of pm^2/Hz) *	Dynamic resolution (fm/$\sqrt{\text{Hz}}$)**
Micron Optics Si155	0.5	-26.4	47.8
Ibsen I-MON USB 512	1.5	-35.3	17.1
Proposed interrogator	280	-46.6	4.7

* Noise levels as retrieved from Fig.8
** Values calculated from the square root of the PSD noise floor.

standard deviation of the difference between the two traces over one period was 3.7 pm, which shows that there is a good agreement between the traces considering that the commercial interrogator has an accuracy of 5 pm. It is worth noting that even though the wavelength sweep spans beyond a full fringe (FSR was 0.94 nm, while the wavelength sweep was ∼1.4 nm), an unwrapping algorithm implemented in PC successfully corrects the cycle discontinuities.

Fig. 11 shows the acquired data at much higher excitation frequencies. Fig. 11(a) and (b) shows a 42-kHz signal, which is the resonance frequency of the piezoelectric actuator, thus providing a very strong signal at high frequency. In that figure, a crosstalk smaller than −60 dB is observed between both channels, demonstrating an excellent channel isolation. Fig. 11(c) and (d) shows a 100-kHz signal, which was much weaker due to the frequency limit of the actuator, but still detectable with an SNR of ∼60 dB.

C. Tolerance to Modulation Depth Variations

The tolerance of our interrogator to modulation depth variation was also tested and the results are shown in Figs. 12 and 13. The Y and X components, which are necessary to compute the phase, as shown in (7), when they are plotted against each other for different phase shifts from 0 to 2π, they should form a circle if there is no distortion, otherwise they form an ellipse [12].

A plot of the Y versus X components for different modulation depths is shown in Fig. 12. For the standard PGC technique, when the C value changes from its nominal value, the circle transforms into an ellipse. Instead, for the MTM technique, the circle does not change shape appreciably for all the variations tested (up to 10.2% variation of C), which implies that this technique is much more robust to modulation depth changes. The effect of distortion on the waveform is shown in Fig. 13 with a 35-Hz sawtooth signal. When C is at its nominal value [see Fig. 13(a)], both techniques show the same retrieved signal. However, when C varies 10.2% below its nominal value [see Fig. 13(b)], the standard PGC technique generates a distortion in the signal which can be seen as a zigzag of the curve at the rising part, whereas for the MTM technique it remains straight, as is undistorted.

D. Variation of FSR

Another feature of our interrogator is the adjustable FSR through the change in the length of the PMF. Fig. 14 shows the spectra of the interferometer for different lengths of PMF. The results only show the length of the prolongation of PMF since the system had already 2 m of PMF. A lower value of FSR provides greater sensitivity, since it requires a smaller change in the wavelength shift from the FBG to cause a 2π phase shift. On the other hand, a greater value of FSR results in an interferometer with a higher range of detection and reduced sensitivity. It is worth mentioning that the wavelength shift can still be recovered for shifts that go beyond the FSR by using a phase unwrapping algorithm that compares the phase with

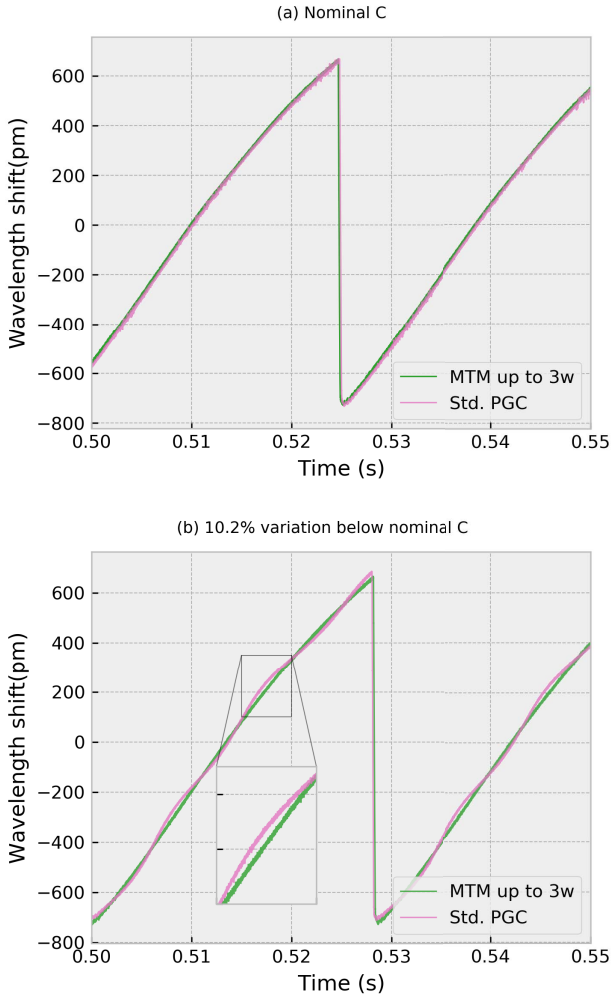

Fig. 13. Comparison between MTM and standard PGC techniques to the tolerance to changes in the modulation depth (C) with a 35-Hz sawtooth signal. As C deviates from its nominal value, the Std PGC technique generates distortion in the retrieved signal which can be seen as a zig-zag pattern. (a) Nominal C. (b) 10.2% variation below nominal C.

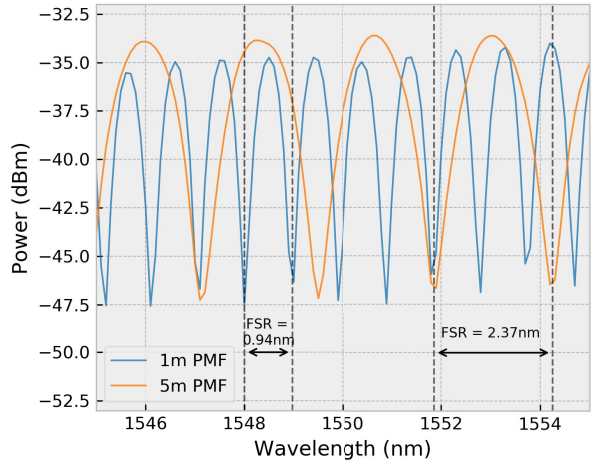

Fig. 14. Sagnac interferometer spectrum for different lengths of PMF. For shorter lengths of PMF, the FSR is reduced, which results in an interferometer with greater sensitivity for the wavelength shift.

its previous value and offsets the trace when two consecutive phase values change more than π. However, in situations

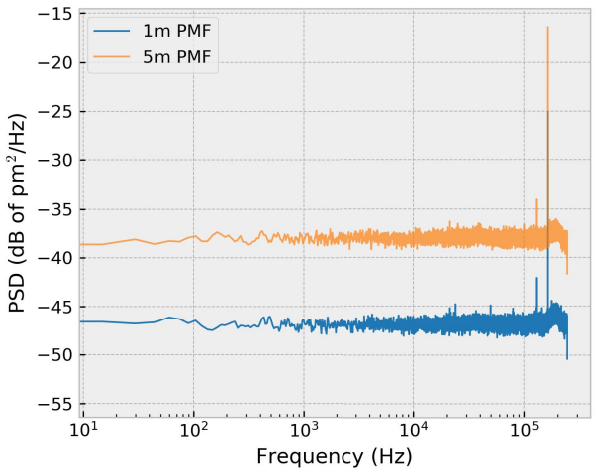

Fig. 15. Wavelength PSD of noise levels for different lengths of PMF: (blue) 1-m PMF, with an FSR = 0.94 nm; (orange) 5-m PMF, with an FSR = 2.37 nm.

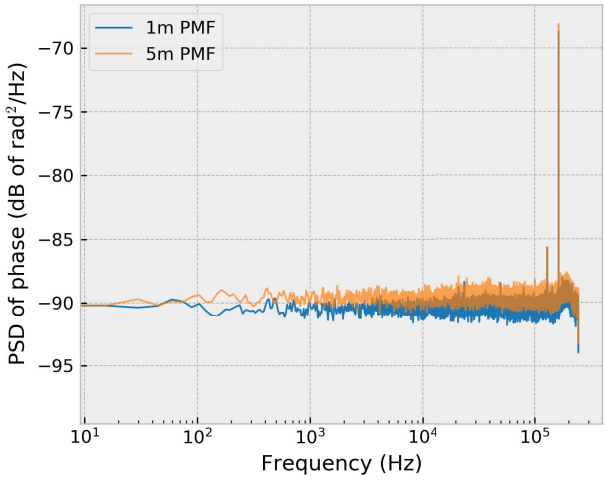

Fig. 16. PSD of phase noise in rad for different lengths of PMF: (blue) 1-m PMF, corresponding to FSR = 0.94 nm; (orange) 5-m PMF, corresponding to FSR = 2.37 nm.

where absolute wavelength measurements are needed with no initial reference, the FSR must be kept higher than the expected range of the FBG.

The wavelength noise for different lengths of PMF is shown in Fig. 15, where the noise level is considerably reduced when changing from 5 to 1 m of PMF. To understand the change in the noise floor, we show in Fig. 16 the phase noise in both cases. The fact that the noise floors are very similar shows that the noise is coming from the phase estimation by the interferometer.

IV. Conclusion

We have shown a high-speed FBG interrogator system which consists of an active Sagnac interferometer which is electro-optically dithered in the MHz range with a lithium niobate modulator. The demodulation scheme is a modified PGC algorithm using the MTM technique to reduce distortion. The signal processing is performed in real time, with a low-cost FPGA system, which streams data to the computer at rates up to 0.98 MS/s. The system demonstrated a dynamic wavelength resolution of 4.7 fm/Hz$^{1/2}$, which was lower than two different

commercial interrogators. The system can monitor two FBGs simultaneously using a single interferometer by wavelength demultiplexing at its output; this allows using one FBG as a reference, so that common noise sources in the interferometer can be canceled. The system bandwidth and sample rate are only limited by the signal processing and data streaming, not by the optical system. This instrument can find applications in scenarios requiring high-speed monitoring at frequencies beyond tens or hundreds of kHz.

REFERENCES

[1] S. Yin, P. B. Ruffin, and F. T. S. Yu, *Fiber Optic Sensors*. Boca Raton, FL, USA: CRC Press, 2008.

[2] P. Lu *et al.*, "Distributed optical fiber sensing: Review and perspective," *Appl. Phys. Rev.*, vol. 6, no. 4, 2019, Art. no. 041302.

[3] R. W. Fallon, L. Zhang, L. A. Everall, J. A. R. Williams, and I. Bennion, "All-fibre optical sensing system: Bragg grating sensor interrogated by a long-period grating," *Meas. Sci. Tech.*, vol. 9, no. 12, p. 1969, 1998.

[4] A. Dandridge, A. B. Tveten, and T. G. Giallorenzi, "Homodyne demodulation scheme for fiber optic sensors using phase generated carrier," *IEEE Trans. Microw. Theory Techn.*, vol. MTT-30, no. 10, pp. 1635–1641, Oct. 1982.

[5] T. A. Berkoff and A. D. Kersey, "Fiber Bragg grating array sensor system using a bandpass wavelength division multiplexer and interferometric detectionn," *IEEE Photon. Technol. Lett.*, vol. 8, no. 11, pp. 1522–1524, Nov. 1996.

[6] C. J. Oton, L. Tozzetti, and F. D. Pasquale, "High-speed FBG interrogation with electro-optically tunable Sagnac loops," *J. Lightw. Technol.*, vol. 38, no. 16, pp. 4513–4519, Aug. 15, 2020.

[7] J. He, L. Wang, F. Li, and Y. Liu, "An ameliorated phase generated carrier demodulation algorithm with low harmonic distortion and high stability," *J. Lightw. Technol.*, vol. 28, no. 22, pp. 3258–3265, Nov. 15, 2010.

[8] A. Zhang and S. Zhang, "High stability fiber-optics sensors with an improved PGC demodulation algorithm," *IEEE Sensors J.*, vol. 16, no. 21, pp. 7681–7684, Nov. 2016.

[9] G. Q. Wang, T. W. Xu, and F. Li, "PGC demodulation technique with high stability and low harmonic distortion," *IEEE Phot. Technol. Lett.*, vol. 24, no. 23, pp. 2093–2096, Dec. 2012.

[10] S. Zhang, Y. Chen, B. Chen, L. Yan, J. Xie, and Y. Lou, "A PGC-DCDM demodulation scheme insensitive to phase modulation depth and carrier phase delay in an EOM-based SPM interferometer," *Opt. Commun.*, vol. 474, Nov. 2020, Art. no. 126183.

[11] Z. Qu, S. Guo, C. Hou, J. Yang, and L. Yuan, "Real-time self-calibration PGC-arctan demodulation algorithm in fiber-optic interferometric sensors," *Opt. Exp.*, vol. 27, no. 16, p. 23593, Aug. 2019.

[12] Y. Marin, P. Velha, and C. J. Oton, "Distortion-corrected phase demodulation using phase-generated carrier with multitone mixing," *Opt. Exp.*, vol. 28, no. 24, pp. 36849–36861, Nov. 2020.

[13] D. E. Zelmon, D. L. Small, and D. Jundt, "Infrared corrected Sellmeier coefficients for congruently grown lithium niobate and 5 mol·% magnesium oxide–doped lithium niobate," *J. Opt. Soc. Amer. B, Opt. Phys.*, vol. 14, pp. 3319–3322, 1997.

[14] M. A. Luda, M. Drechsler, C. T. Schmiegelow, and J. Codnia, "Compact embedded device for lock-in measurements and experiment active control," *Rev. Sci. Instrum.*, vol. 90, no. 2, 2019, Art. no. 023106.

[15] R. Pitaya. *Scope V0.95*. Accessed: Oct. 12, 2021. [Online]. Available: https://github.com/RedPitaya/RedPitaya/tree/release-v0.95/apps-free/scope

Javier Elaskar was born in Córdoba, Argentina, in 1994. He received the M.Sc. degree in electronic engineering from the Universidad Nacional de Córdoba, Córdoba, in 2018, and the joint master's degree in photonics and networking from the Scuola Superiore Sant'Anna, Pisa, Italy, and Aston University, Birmingham, U.K., in 2021. He is currently pursuing the Ph.D. degree in emerging digital technologies with the Scuola Superiore Sant'Anna, with research topics related with optical fiber sensors and photonic devices.

Marcelo A. Luda was born in Argentina in 1985. He received the Ph.D. degree from the National University of Buenos Aires, Buenos Aires, Argentina, in 2021.

He has been teaching as a Professorship Assistant and the Chief of laboratory practical works with the National University of Buenos Aires since 2011 and 2019, respectively. In 2011, he joined the CITEDEF Laser Department (dependent on the Ministry of Defense), Buenos Aires, where he worked with Quantum Optics (up to 2013) and in the Molecular Lasers Divisions (to this day). His current research topics include laser applications in metrology and field-programmable gate array (FPGA) instrumentation for physics laboratories.

Lorenzo Tozzetti was born in Florence, Italy, in 1982. He received the bachelor's degree in physics and the master's degree in astrophysics from the University of Florence, Florence, in 2009 and 2017, respectively.

From 2009 to 2011, he has worked as a Research Fellow on the production of cosmic dust analogs with the Department of Physics and Astronomy, University of Florence. From 2011 to 2014, he has worked as a Research Fellow with the INAF–Astrophysical Observatory of Arcetri, Florence, focusing on the characterization of cosmic dust analogs. In the following two years, he further developed the same topics at the University of Florence. From 2016 to 2017, he has worked with the National Research Council of Italy (CNR)–National Institute of Optics (INO), Florence, on the development of a prototype for the analysis of the composition of planetary atmospheres. Since 2018, he has been working as a Research Fellow with the Institute of Mechanical Intelligence (IIM), Scuola Superiore Sant'Anna, Pisa, Italy, with particular interest on optical fiber sensors and silicon photonics.

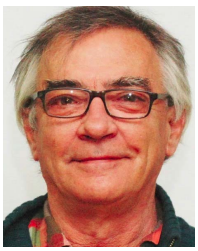

Jorge Codnia was born in Argentina in 1960. He received the Ph.D. degree from the National University of Buenos Aires, Buenos Aires, Argentina, in 2007.

He is currently an Adjunct Professor with the Institute of Sciences, National University of General Sarmiento, Buenos Aires. In 1993, he joined the CITEDEF Laser Department (dependent on the Ministry of Defense), Buenos Aires. In 2007, he was the Head of the Molecular Lasers Division whose current lines of research are, on one hand, theoretical and experimental studies in molecular physics for isotopic laser enrichment, and on the other, development of stabilized laser systems with applications in metrology.

Claudio J. Oton was born in 1978. He received the Ph.D. degree from the University of La Laguna, Tenerife, Spain, in 2005.

Then, he spent four years with the Optoelectronics Research Centre, Southampton, U.K., where he has worked on integrated optical amplifiers and lasers on silicon as a Marie Curie Post-Doctoral Fellow. In 2009, he joined the Nanophotonics Technology Center, Universidad Politecnica de Valencia, Valencia, Spain, where he studied nonlinear silicon photonic devices. Since 2012, he has been an Assistant Professor with the Scuola Superiore Sant'Anna, Pisa, Italy. He is the author of more than 130 journal articles and conference papers, with more than 2000 citations and an H-index of 26. His current research topics include optical fiber sensors and silicon photonics-integrated devices.